

Marked clustering statistics in $f(R)$ gravity cosmologies

César Hernández-Aguayo,[★] Carlton M. Baugh and Baojiu Li

Institute for Computational Cosmology, Department of Physics, Durham University, South Road, Durham DH1 3LE, UK

Accepted 2018 July 5. Received 2018 June 18; in original form 2017 November 17

ABSTRACT

We analyse the two-point and marked correlation functions (mCFs) of haloes and galaxies in three variants of the chameleon $f(R)$ gravity model using N -body simulations, and compare to a fiducial Λ cold dark matter model based on general relativity (GR). Using a halo occupation distribution (HOD) prescription, we populate dark matter haloes with galaxies, where the HOD parameters have been tuned such that the galaxy number densities and the real-space galaxy two-point correlation functions in the modified gravity models match those in GR to within 1–3 per cent. We test the idea that since the behaviour of gravity is dependent on environment, mCFs may display a measurable difference between the models. For this we test marks based on the density field and the Newtonian gravitational potential. We find that the galaxy mCF shows significant differences measured in different models on scales smaller than $r \lesssim 20 h^{-1}$ Mpc. Guided by simulations to identify a suitable mark, this approach could be used as a new probe of the accelerated expansion of the Universe.

Key words: gravitation – methods: data analysis – methods: statistical – large-scale structure of Universe – cosmology: theory.

1 INTRODUCTION

The Λ cold dark matter (Λ CDM) model is currently the most widely accepted description of the Universe (e.g. see Ade et al. 2014). In this model small ripples in the density of the Universe at early times, seeded during a period of rapid expansion called inflation, were boosted by gravity to form the cosmic web of voids, galaxies, and clusters of galaxies that we see today. The Λ CDM model works remarkably well on large scales, with the highlight being the prediction of the temperature fluctuations in the cosmic microwave background (CMB) radiation (e.g. Ade et al. 2016). However, the model arguably runs into difficulties on small scales, which could be related to the nature of the dark matter particle or could be solved by appealing to the physics of galaxy formation (for a review see Weinberg et al. 2014).

Several large international survey projects are underway which aim to determine what is behind the accelerating expansion of the Universe, such as the Dark Energy Survey (DES) (Dark Energy Survey Collaboration 2016), the Dark Energy Spectrographic Instrument (DESI) survey (Aghamousa et al. 2016), and the European Space Agency’s Euclid mission (Laureijs et al. 2011). These surveys aim to make ambitious measurements which, for the first time, will be dominated by systematics rather than by the volume of the Universe surveyed. Accurate theoretical predictions are urgently required to compare with these expected measurements and to rule out competing scenarios for the accelerating cosmic expansion.

Theoretically, the Λ CDM model is somewhat unappealing due to the presence of the cosmological constant, the agent behind the accelerating cosmic expansion. The magnitude of the cosmological constant is hard to motivate from a particle physics perspective. There is also a ‘Why now?’ problem: a strong coincidence seems to be required for us to be at the right point in cosmic history to experience comparable energy densities in matter and the cosmological constant, with the latter dominating the current expansion. As a result, alternatives to the cosmological constant have been studied extensively in recent years: one possibility is adding more matter species to the energy-momentum tensor (the so-called dark energy models; see e.g. Copeland, Sami & Tsujikawa 2006); on the other hand there are models that change the left-hand side of Einstein’s equations (these models are called modified gravity models; for reviews see Joyce et al. 2015; Koyama 2016).

Here, we focus our attention on a particular class of modified gravity models – Hu & Sawicki (2007) chameleon $f(R)$ gravity. This model is obtained by adding a general function of the Ricci scalar, $f(R)$, to the Einstein–Hilbert action. This modification gives rise to a new scalar degree of freedom in gravity (Carroll et al. 2004). In order to recover general relativity (GR), the new scalar field becomes massive in high-density regions (i.e. the Solar system) and its interactions are suppressed by the so-called chameleon screening mechanism (Khoury & Weltman 2004).

The standard tool to model the growth of large-scale structure into the non-linear regime is N -body simulation. In order to robustly test gravity on cosmological scales, reliable N -body simulations of modified gravity models are essential. The non-linear nature of the scalar field equation requires the implementation of novel

[★] E-mail: cesar.hernandez-aguayo@durham.ac.uk

numerical techniques, which is what makes N -body simulations of modified gravity challenging (Barreira, Bose & Li 2015; Winther et al. 2015; Bose et al. 2017). Once such simulations are ready, we can use measurements of clustering statistics from surveys to test and constrain cosmological models (see e.g. Reid et al. 2010).

Several recent works have studied clustering in $f(R)$ gravity. For example, Li et al. (2013) predicted the matter and velocity divergence power spectra and their time evolution measured from several large-volume N -body simulations with varying box sizes and resolution. Jennings et al. (2012) predicted the clustering of dark matter in redshift space, finding significant deviations from the clustering signal in standard gravity, with an enhanced boost in power on large scales, and stronger damping on small scales in the $f(R)$ models compared to GR at redshifts $z < 1$. More recently, Arnalte-Mur, Hellwing & Norberg (2017) compared the time evolution of the two-point correlation function of dark matter haloes in real and redshift space in modified gravity and GR.

An approach related to the two-point correlation function has been proposed to test modified gravity models, called the marked correlation function (mCF) (Sheth, Connolly & Skibba 2005). Marked statistics offer the possibility of testing how galaxy properties correlate with environment. Previous applications of the mCF range from the analysis of the environmental dependence of bars and bulges in disc galaxies (see e.g. Skibba et al. 2012) to breaking degeneracies in halo occupation distribution (HOD) modelling (White & Padmanabhan 2009).

White (2016) proposed that marked statistics might provide a means to distinguish between modified gravity models and GR, due to the environmental dependence of the strength of gravity (for earlier work on environmental dependence in modified gravity; see e.g. Zhao, Li & Koyama 2011; Winther, Mota & Li 2012; Lombriser, Simpson & Mead 2015; Shi, Li & Han 2017). Marks can be designed which down-weight high-density regions, for which modifications to gravity are screened, and up-weight low-density, unscreened regions to maximize the differences in the clustering signal. Valogiannis & Bean (2017) tested this idea by using the dark matter particle distribution from N -body simulations of symmetron and $f(R)$ modified gravity models. In the case of $f(R)$ gravity with $|f_{R0}| = 10^{-4}$, they found a maximum difference of 37 per cent with respect to GR. Armijo et al. (2018) studied the galaxy mCF by up-weighting low and high-density regions using marks in function of the galaxy density field and the host halo mass of galaxies, they found significant differences between the $f(R)$ and GR models. Here, we focus our attention on the clustering of dark matter haloes and HOD galaxies for $f(R)$ gravity models to make a more direct connection with observations.

This paper is organized as follows. In Section 2, we give a brief review of the theoretical description of $f(R)$ gravity and the physical motivation behind this model. Section 3 explains the numerical set-up of the simulations and the generation of halo and galaxy catalogues. The main results are presented in Section 4. Finally, in Section 5, we present a brief discussion and our general conclusions.

2 $f(R)$ GRAVITY THEORY

A popular family of modified gravity models is obtained by replacing the Ricci scalar R in the usual Einstein–Hilbert Lagrangian density by some function $f(R)$ (see De Felice & Tsujikawa 2010; Sotiriou & Faraoni 2010; for recent reviews). These models are often considered as an alternative solution for the accelerating cosmic expansion. However, it should be noted that they are able to accelerate the expansion only because a cosmological constant is added

‘through the back door’ (Brax et al. 2008; Wang, Hui & Khoury 2012; Ceron-Hurtado, He & Li 2016), and so they do not offer a real solution to the cosmological constant problem. Nevertheless, they constitute a representative model with which to study cosmological constraints on possible deviations from GR.

2.1 Theoretical framework

The action of $f(R)$ theories is given by (Carroll et al. 2004)

$$S = \int d^4x \sqrt{-g} \frac{1}{16\pi G} (R + f(R)) + S_m(g_{\mu\nu}, \psi_i), \quad (1)$$

where G is Newton’s constant, g is the determinant of the metric $g_{\mu\nu}$ and S_m is the action of the matter fields ψ_i (including the contributions from cold dark matter, baryons, radiation, and neutrinos).

Varying the action given in equation (1), with respect to the metric, $g_{\mu\nu}$, one obtains the modified Einstein equations

$$G_{\mu\nu} + f_R R_{\mu\nu} - g_{\mu\nu} \left(\frac{1}{2} f(R) - \square f_R \right) - \nabla_\mu \nabla_\nu f_R = 8\pi G T_{\mu\nu}^m, \quad (2)$$

where $G_{\mu\nu} = R_{\mu\nu} - \frac{1}{2} g_{\mu\nu} R$ is the Einstein tensor, ∇_μ is the covariant derivative, $\square = \nabla^\mu \nabla_\mu$ the d’Alembertian, and $T_{\mu\nu}^m$ is the energy–momentum tensor for matter. Here

$$f_R \equiv \frac{df(R)}{dR}, \quad (3)$$

is the extra degree of freedom of this model, known as the *scalaron* field.

Taking the trace of equation (2), we obtain the equation of motion for the scalaron field,

$$\square f_R = \frac{1}{3} (R - f_R R + 2f(R) + 8\pi G \rho_m), \quad (4)$$

where ρ_m is the matter density of the Universe.

Since we are interested in the cosmological evolution of the model, we derive the perturbation equations using the flat Friedmann–Robertson–Walker (FRW) metric in the Newtonian gauge

$$ds^2 = (1 + 2\Psi)dt^2 - a^2(t)(1 - 2\Phi)\gamma_{ij}dx^i dx^j, \quad (5)$$

where Ψ and Φ are the gravitational potentials, t is the cosmic time, x^i represent the comoving coordinates, γ_{ij} is the 3D metric, and a is the scale factor, with $a(t_0) = a_0 = 1$ at the present time.

In the quasi-static and weak field limits (Bose, Hellwing & Li 2015), structure formation in this model is determined by the following equations:

$$\nabla^2 \Phi = \frac{16\pi G}{3} a^2 \delta\rho_m + \frac{1}{6} a^2 \delta R, \quad (6)$$

$$\nabla^2 f_R = -\frac{a^2}{3} [\delta R + 8\pi G \delta\rho_m], \quad (7)$$

in which ∇^2 is the three-dimensional Laplacian operator, $\delta\rho_m = \rho_m - \bar{\rho}_m$ and $\delta R = R(f_R) - \bar{R}$ are, respectively, the density and Ricci scalar perturbations (overbars denote background cosmological quantities).

2.2 The chameleon mechanism

In $f(R)$ gravity the modifications to Newtonian gravity can be considered as a fifth force mediated by the scalaron field, f_R . The chameleon

mechanism (see e.g. Khoury & Weltman 2004; Mota & Shaw 2007) was introduced to give scalar fields an environment-dependent effective mass allowing the scalar mediated force to be suppressed under certain environmental conditions.

Because the scalaron field itself is massive, this fifth force is of Yukawa type, i.e. decaying exponentially as $\exp(-m_{\text{eff}}r)$, where m_{eff} is the scalaron mass

$$m_{\text{eff}}^2 \equiv \frac{d^2 V_{\text{eff}}}{df_R^2}, \quad (8)$$

and the effective potential is related to the trace of the modified Einstein equation (4)

$$\frac{dV_{\text{eff}}}{df_R} = \frac{1}{3}(R - f_R R + 2f(R) + 8\pi G \rho_m). \quad (9)$$

In $f(R)$ gravity this fifth force enhances gravity in regions of weak gravitational potential and on scales below the Compton wavelength of the scalar field, $\lambda = m_{\text{eff}}^{-1}$. While in high-density regions, m_{eff} is heavy and the fifth force is more strongly suppressed and gravity reverts to GR.

2.3 The Hu-Sawicki model

We consider the Hu & Sawicki model

$$f(R) = -m^2 \frac{c_1}{c_2} \frac{(-R/m^2)^n}{(-R/m^2)^n + 1}, \quad (10)$$

where m is a characteristic mass scale, defined by $m^2 = 8\pi G \bar{\rho}_{m0}/3 = H_0^2 \Omega_m$, Ω_m is the cosmological matter density parameter, H_0 is the present-day value of the Hubble parameter, and n , c_1 and c_2 are dimensionless parameters of the model. The scalaron field, equation (3), takes the form

$$f_R = -\frac{c_1}{c_2} \frac{n(-R/m^2)^{n-1}}{[(-R/m^2)^n + 1]^2}. \quad (11)$$

To match the background expansion to that in the Λ CDM model, we set

$$\frac{c_1}{c_2} = 6 \frac{\Omega_\Lambda}{\Omega_m}, \quad (12)$$

where $\Omega_\Lambda \equiv 1 - \Omega_m$.

The expression of the scalaron field, equation (11), simplifies when the background value of the Ricci scalar satisfies $|\bar{R}| \gg m^2$. From

$$-\bar{R} \approx 8\pi G \bar{\rho}_m - 2f(\bar{R}) \approx 3m^2 \left[a^{-3} + \frac{2}{3} \frac{c_1}{c_2} \right], \quad (13)$$

when $\Omega_\Lambda \approx 0.7$ and $\Omega_m \approx 0.3$, we find $|\bar{R}| \approx 40m^2 \gg m^2$. Thus

$$f_R \approx -n \frac{c_1}{c_2} \left(\frac{m^2}{-R} \right)^{n+1}. \quad (14)$$

The model then has two remaining free parameters, n and c_1/c_2^2 . The latter is related to the present-day value of the background scalaron, f_{R0} ,

$$\frac{c_1}{c_2^2} = -\frac{1}{n} \left[3 \left(1 + 4 \frac{\Omega_\Lambda}{\Omega_m} \right) \right]^{n+1} f_{R0}. \quad (15)$$

Hence, the choice of f_{R0} and n fully specifies the model. Here we focus on the case of $n = 1$, which is the most well-studied case in the literature.

Table 1. Numerical parameters of the simulations used.

Labels	GR, F6, F5, F4
Present value of the scalaron field	$ f_{R0} = 0, 10^{-6}, 10^{-5}, 10^{-4}$
Box size	$L_{\text{box}} = 1024 h^{-1} \text{ Mpc}$
Number of DM particles	$N_p = 1024^3$
Mass of DM particle	$m_p = 7.798 \times 10^{10} h^{-1} M_\odot$
Initial redshift	$z_{\text{in}} = 49$
Final redshift	$z_{\text{fi}} = 0$
Realisations	5
<i>Cosmological parameters:</i>	
Total matter density	$\Omega_m = 0.281$
$1 - \Omega_m$	$\Omega_\Lambda = 0.719$
Baryonic matter density	$\Omega_b = 0.046$
Cold dark matter density	$\Omega_{\text{cdm}} = 0.235$
Dimensionless Hubble parameter	$h = 0.697$
Primordial power spectral index	$n_s = 0.971$
rms linear density fluctuation	$\sigma_8 = 0.820$

3 SIMULATIONS AND HALO/GALAXY CATALOGUES

Here we present a description of the simulations used, the construction of halo catalogues, and the HOD prescription used to populate dark matter haloes with galaxies.

3.1 Numerical simulations

As we are interested in the effects of $f(R)$ gravity on large scales, we choose three Hu-Sawicki models with $n = 1$ and $|f_{R0}| = 10^{-6}, 10^{-5}, 10^{-4}$ (which we hereafter refer to as F6, F5 and F4, respectively) and the Λ CDM model which assumes GR. Despite the observational tensions faced by $f(R)$ models with $|f_{R0}| > 10^{-5}$ (see e.g. Lombriser 2014; Cataneo et al. 2015; Liu et al. 2016) it is interesting to consider a wide range of $f(R)$ models to study their impact on the halo/galaxy clustering.

We use the ELEPHANT (Extended LEnsing PHysics using ANalytic ray Tracing) simulations executed using the code ECOSMOG (Li et al. 2012), which is based on the adaptive mesh refinement (AMR) N -body code RAMSES (Teyssier 2002). Table 1 lists the properties of the simulations used in our analysis. The cosmological parameters were adopted from the best-fitting values to the WMAP 9 yr CMB measurements (Hinshaw et al. 2013). All simulations use $N_p = 1024^3$ particles with a mass of $m_p = 7.798 \times 10^{10} h^{-1} M_\odot$ to follow the evolution of the dark matter distribution in a volume of $V_{\text{box}} = (1024 h^{-1} \text{ Mpc})^3$. The initial conditions were generated at $z_{\text{ini}} = 49$ using the MPGRAFIC code (Prunet et al. 2008). All simulations were run using the same initial conditions up to the present time, $z_{\text{fi}} = 0$, generating 37 + 1 snapshots. Here, we analyse the outputs at $z = 0.5$.

3.2 Halo catalogues and mass function

Dark matter haloes are the building blocks of large-scale structure and the hosts of galaxies. Therefore, the study of their statistical properties, such as their abundance and clustering, is of great importance in understanding the nature of gravity. The halo catalogues were produced using the ROCKSTAR halo finder code (Behroozi,

Wechsler & Wu 2013). ROCKSTAR calculates halo masses using the spherical overdensity (SO) approach (Cole & Lacey 1996), including all particles and substructures in the halo. We keep only the ‘parent’ halo, omitting other substructures from our analysis.

We define the mass of a halo as M_{200c} , the mass within a sphere of radius r_{200c} , which is the radius within which the mean overdensity is 200 times the critical density of the universe ρ_c .

$$M_{200c} = \frac{4\pi}{3} 200 \rho_c r_{200c}^3. \quad (16)$$

The dark matter halo mass function (HMF) quantifies the number density of dark matter haloes as a function of their mass. The HMF is sensitive to the cosmological parameters, Ω_m , Ω_Λ , and σ_8 , and to modifications to gravity. The Λ CDM model predicts an HMF in which the number of haloes increases with decreasing halo mass. $f(R)$ models predict more haloes than the Λ CDM model at almost all masses due to the enhancement of gravity. Theoretically, the HMF is given by (Press & Schechter 1974)

$$\frac{dn}{dM_{200c}} = f(\sigma) \frac{\bar{\rho}_m}{M_{200c}^2} \left| \frac{d \ln \sigma^{-1}}{d \ln M_{200c}} \right|, \quad (17)$$

where σ is the linear theory variance in the matter perturbation, $\bar{\rho}_m$ is the mean density of the Universe and $f(\sigma)$ is an analytical fitting formula. The cumulative number density of haloes above the mass M_{200c} is

$$n(> M_{200c}) = \int_{M_{200c}}^{\infty} \frac{dn}{d \log_{10} M_{200c}} d \log_{10} M_{200c}. \quad (18)$$

We compare the fitting formula of Tinker et al. (2010; hereafter **Tinker10**) to the simulation results. **Tinker10** calibrated their fitting formula using an SO algorithm to identify dark matter haloes in numerical simulations which is consistent with the approach used in ROCKSTAR. The analytical predictions were computed by using the online tool **HMFCALC**¹ (Murray, Power & Robotham 2013).

Fig. 1 shows the cumulative halo mass function (cHMF) measured from the simulations and the relative difference between the $f(R)$ models and GR at $z = 0.5$. As expected, the largest deviation from GR is displayed by the F4 model (red line; Schmidt et al. 2009; Lombriser et al. 2013; Cataneo et al. 2016). The lower panel of Fig. 1 shows that the cHMF in the F4 model reaches a difference with respect to GR of >50 percent for haloes of mass $M_{200c} > 10^{14.3} h^{-1} M_\odot$. The maximum difference found between F5 (green line) and GR reaches 25 percent for haloes with mass $M_{200c} \approx 10^{13.2} h^{-1} M_\odot$. On the other hand, for the F6 model (blue line) we see that for very massive haloes, the HMF is the same as that in GR. This is because the chameleon mechanism works efficiently for such haloes to suppress the effects of the enhancement to gravity. These differences are purely the result of the modified gravitational force in $f(R)$ models. The stronger deviation of F4 from GR is due to the inefficient screening mechanism in this model compared to the screening in the F6 model.

To make a direct comparison between the halo and galaxy clustering we select a halo population from the simulations by fixing the halo number density (in this case we take the number density of the BOSS-CMASS-DR9 sample at $z = 0.5$, $n_h = n_g = 3.2 \times 10^{-4} h^3 \text{ Mpc}^{-3}$; Anderson et al. 2012) and selecting haloes above the mass threshold corresponding to that number density. The horizontal dashed line in Fig. 1 corresponds to the halo number density used to define our halo sample. The minimum mass that

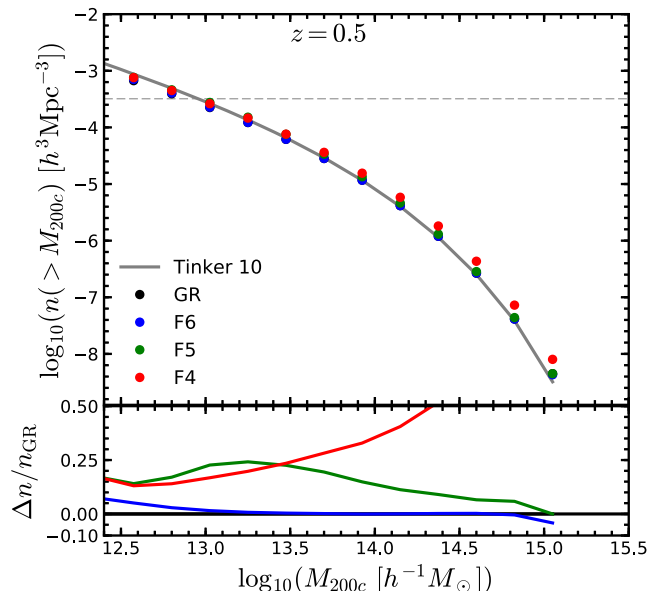


Figure 1. The cHMF in the models at $z = 0.5$. Different colours represent different models, as labelled. The values for each model correspond to the average over the five realisations. The horizontal dashed line shows the number density we use to define our halo sample ($n_h = 3.2 \times 10^{-4} h^3 \text{ Mpc}^{-3}$). The grey curve shows the **Tinker10** cHMF for GR at $z = 0.5$. The lower panel shows the relative difference with respect to the Λ CDM (GR) model.

defines the halo sample for each model is: $7.643 \times 10^{12} h^{-1} M_\odot$ (GR), $7.798 \times 10^{12} h^{-1} M_\odot$ (F6), $9.124 \times 10^{12} h^{-1} M_\odot$ (F5), and $8.734 \times 10^{12} h^{-1} M_\odot$ (F4). The fact that F5 has a higher minimum mass is because this model produces more haloes with mass $M_{200c} \sim 10^{13} h^{-1} M_\odot$ (as we can see from the lower panel of Fig. 1) than F6 and F4. For F4, many of the medium-mass haloes have merged to form more massive haloes, hence this model predicts fewer smaller haloes than F5.

3.3 HOD prescription and galaxy catalogues

To compare the simulations with observations one has to populate dark matter haloes with galaxies. This can be done using one of a number of empirical techniques depending on the physical application we are interested in, such as subhalo abundance matching (Vale & Ostriker 2004; Conroy, Wechsler & Kravtsov 2006; Klypin et al. 2013; Reddick et al. 2013), the conditional luminosity function (Yang, Mo & van den Bosch 2003; Cooray & Milosavljevic 2005), or the HOD (Berlind & Weinberg 2002; Kravtsov et al. 2004; Zheng et al. 2005). These empirical descriptions of the galaxy-halo connection have the flexibility to give accurate reproductions of observational estimates of galaxy clustering. A second, more expensive but physically motivated method is hydrodynamical simulation (Vogelsberger et al. 2014; Schaye et al. 2015). A third possibility, which retains the physical basis of hydrodynamical simulation at a fraction of the computational cost is semi-analytical modelling of galaxy formation (Somerville & Primack 1999; Cole et al. 2000; Baugh 2006; Benson 2010) in which an N -body dark matter-only simulation is populated with galaxies after solving a set of coupled differential equations. To date, little work has been done to study galaxy formation and clustering in modified gravity models (see Fontanot et al. 2013 for an example), so here we will resort to the empirical approach of HOD modelling.

¹<http://hmf.icrar.org/>

We populate haloes using a functional form for the HOD (Peacock & Smith 2000; Berlind & Weinberg 2002) with five parameters, as used by Zheng, Coil & Zehavi (2007).

In this form, the mean number of galaxies in a halo of mass M_h (in our case $M_h = M_{200c}$) is the sum of the mean number of central galaxies plus the mean number of satellite galaxies

$$\langle N(M_h) \rangle = \langle N_c(M_h) \rangle + \langle N_s(M_h) \rangle, \quad (19)$$

$$\langle N_c(M_h) \rangle = \frac{1}{2} \left[1 + \operatorname{erf} \left(\frac{\log_{10} M_h - \log_{10} M_{\min}}{\sigma_{\log M}} \right) \right], \quad (20)$$

$$\langle N_s(M_h) \rangle = \langle N_c(M_h) \rangle \left(\frac{M_h - M_0}{M_1} \right)^\alpha, \quad (21)$$

and $\langle N_s(M_h) \rangle = 0$ if $M_h < M_0$. $\langle N_{c/s}(M_h) \rangle$ is the average number of central or satellite galaxies, respectively, in a halo of mass M_h . The model depends on five parameters: M_{\min} , M_0 , M_1 , $\sigma_{\log M}$, and α . From equations (20) and (21) we can see that M_{\min} and M_0 represent the halo mass threshold to host one central or one satellite galaxy, respectively. Also, we assume that central galaxies are placed at the centre of their host haloes and satellite galaxies are orbiting inside haloes with $M_h \geq M_0$. The satellite galaxies are radially distributed, between $r = [0, r_{200c}]$, following the Navarro–Frenk–White (NFW) profiles of their host halo (Navarro, Frenk & White 1996, 1997).

We generate five galaxy catalogues (one for each independent realisation of the density field) for every gravity model following the prescription described above. The galaxy catalogues match the galaxy number density of the BOSS-CMASS-DR9 sample at $z = 0.5$ ($n_g = 3.2 \times 10^{-4} h^3 \text{Mpc}^{-3}$; Anderson et al. 2012) and the galaxy two-point correlation function across all gravity models (more details are presented below). The BOSS-CMASS sample is dominated by LRGs which are massive galaxies typically residing in haloes with $M_h \sim 10^{13} h^{-1} M_\odot$ (Anderson et al. 2012). Hence, given the mass resolution of the ELEPHANT simulations, these runs are suitable to study the impact of $f(R)$ gravity on galaxy clustering.

The values of the HOD parameters used to populate the GR simulations are those inferred from the abundance and clustering measured for the BOSS-CMASS-DR9 galaxy sample (Manera et al. 2012)

$$\begin{aligned} \log_{10}(M_{\min}/[h^{-1} M_\odot]) &= 13.09, \\ \log_{10}(M_1/[h^{-1} M_\odot]) &= 14.00, \\ \log_{10}(M_0/[h^{-1} M_\odot]) &= 13.077, \\ \sigma_{\log M} &= 0.596, \\ \alpha &= 1.0127. \end{aligned} \quad (22)$$

To find the $f(R)$ HOD parameters, we use the simplex algorithm of Nelder & Mead (1965) to search through the five-dimensional parameter space. We start the algorithm with an initial guess at the values of the HOD parameters, then the code walks through the five-dimensional HOD parameter space looking for the values that minimize the root-mean-square difference (*rms*) of the two-point correlation function between $f(R)$ and GR models. We measure the correlation function using 40 logarithmically spaced radial bins between 1 and 80 h^{-1} Mpc. The fractional difference of the galaxy number density is also included (with a weight of 8) in the *rms* value calculated in order to ensure similar numbers of galaxies in all catalogues. We stop the search when *rms* < 0.02 (this means that the overall agreement is better than 2 percent). For the F4 model, the minimum value of the *rms* we could obtain in practice was ~ 0.03 .

Here, we are interested in the mCF, which was proposed to highlight the environmental dependence in modified gravity models (White 2016). Hence, the most natural choice is to make the unmarked two-point correlation functions (2PCFs) of the different models as close to each other as possible; otherwise when there is a difference in their mCFs we cannot be sure how much of this is due to the different 2PCFs.

The $f(R)$ HOD parameters were tuned for each model and realisation to match the clustering displayed in the counterpart simulation from the GR suite. The best-fitting values of the HOD parameters for the different realisations are listed in Table 2. The variation in the best-fitting parameter values is larger as the modification to gravity increases. We note that, despite the differences between the values of the best-fitting parameters between different models and realisations, the resulting correlation functions and galaxy number densities agree with the GR results to within our target accuracy.

Note that the HOD parameters are degenerate to some extent, so that a comparison of the values of any single parameter across realisations or models should not be overinterpreted. For instance, consider the parameter α that governs the number of satellite galaxies in haloes of a given mass: in the case of the most extreme model, F4, the variation between realisations is ~ 3 per cent. This difference is small compared with the 1σ scatter of HOD parameter fittings, e.g. White et al. (2011).

The left-hand panel of Fig. 2 shows the HOD for CMASS galaxies at $z = 0.5$. The gradual transition from zero to one galaxy per halo is determined by the values adopted for $\log M_{\min}$ and $\sigma_{\log M}$ for central galaxies (dashed lines). The appearance of satellites in haloes (dotted lines) is dictated by the values of M_1 and M_0 , and the rapid increase in the satellite content of haloes with increasing halo mass is governed by α . The HOD parameters are adjusted in the $f(R)$ models to approximately reproduce the abundance and clustering of CMASS galaxies realised in GR. We note that the resulting HODs are very similar between $f(R)$ gravity and GR.

The right-hand panel of Fig. 2 shows the distribution of the number of galaxies as a function of the host halo mass (M_{200c}). We see that most galaxies are found in haloes with mass $10^{13} < M_{200c}/[h^{-1} M_\odot] < 10^{14}$. We also note that the F5 and F4 models produce more galaxies than GR and F6 in this mass range. This is because the abundance of haloes in this mass range is boosted in F5 and F4, as we can see from the relative differences of the cHMFs presented in the lower panel of Fig. 1. Analysing the distribution of galaxies, we find good agreement between the five realisations.

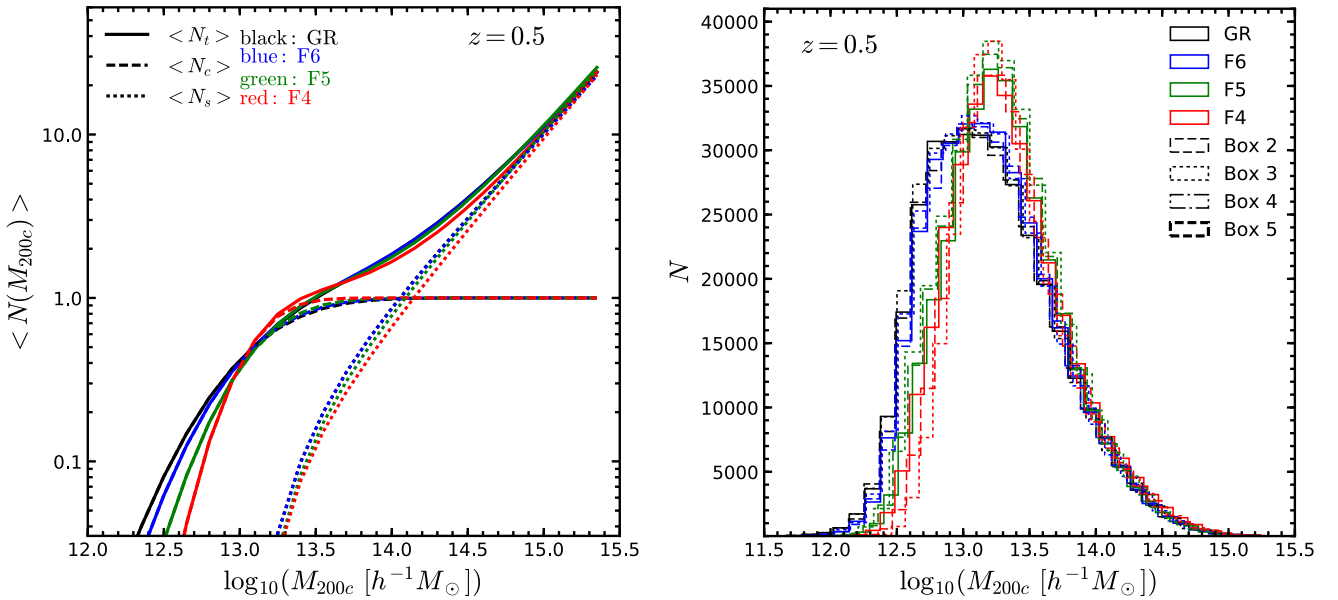
From the distribution of galaxies as a function of host halo mass plotted in Fig. 2, we note that ≈ 0.1 per cent galaxies reside in poorly resolved haloes ($M_{200c} < 10^{12} h^{-1} M_\odot$). The inclusion of these galaxies in the final catalogues does not affect the clustering results.

4 RESULTS

Upcoming galaxy surveys will allow us to measure the clustering of galaxies to an unprecedented level of accuracy with the aim of developing a better understanding of the nature of dark matter, dark energy, and the evolution of galaxies through cosmic time. In this section, we present the statistical tools which can be used to characterize the halo and galaxy distributions in different gravity models. This is the first time that the halo and galaxy clustering has been studied to this level of detail in $f(R)$ gravity models.

Table 2. Values of the HOD parameters (columns 2–6) for $f(R)$ models (F6, F5, F4) at $z = 0.5$ and different realisations (Box 1 – Box 5).

	$\log_{10}(M_{\min}/[h^{-1} M_{\odot}])$	$\log_{10}(M_1/[h^{-1} M_{\odot}])$	$\log_{10}(M_0/[h^{-1} M_{\odot}])$	$\sigma_{\log M}$	α
F6 (Box 1)	13.092	14.004	13.082	0.538	1.0125
F6 (Box 2)	13.093	14.004	13.081	0.539	1.0128
F6 (Box 3)	13.092	14.006	13.083	0.554	1.0131
F6 (Box 4)	13.093	14.002	13.082	0.545	1.0132
F6 (Box 5)	13.094	14.008	13.078	0.547	1.0129
F5 (Box 1)	13.101	14.050	13.077	0.434	1.0643
F5 (Box 2)	13.100	14.045	13.078	0.449	1.0674
F5 (Box 3)	13.134	14.043	13.085	0.525	1.0982
F5 (Box 4)	13.110	14.041	13.078	0.470	1.0710
F5 (Box 5)	13.108	14.041	13.080	0.462	1.0440
F4 (Box 1)	13.084	14.092	13.076	0.394	1.0921
F4 (Box 2)	13.075	14.113	13.073	0.345	1.0804
F4 (Box 3)	13.063	14.113	13.072	0.333	1.0974
F4 (Box 4)	13.076	14.109	13.070	0.353	1.1110
F4 (Box 5)	13.053	14.105	13.075	0.290	1.1143


Figure 2. Left-hand panel: The mean number of central and satellite galaxies as a function of halo mass, $\langle N_{c/s}(M_{200c})$. Dashed lines show the HOD for central galaxies and dotted lines show satellite galaxies while solid lines represent the total averaged number of galaxies, calculated from equations (19) – (21) with parameters (22) for GR and the result of Box 1 listed in Table 2 for the $f(R)$ models, as labelled. Right-hand panel: the number of galaxies in the simulation as a function of the host halo mass, the same distribution at $z = 0.5$ for different realisations: Box 1 (solid lines), Box 2 (dashed lines), Box 3 (dotted lines), Box 4 (dashed–dotted lines), and Box 5 (thick-dashed lines).

4.1 Two-point correlation function

To characterize the clustering of dark matter haloes and galaxies, we use the two-point correlation function, $\xi(r)$. This is defined as the excess probability, compared with that expected for a random distribution, of finding two haloes (or galaxies) contained in volume elements dV_1 and dV_2 at a separation r (Peebles 1980)

$$dP_{12}(r) \equiv \bar{n}^2 [1 + \xi(r)] dV_1 dV_2, \quad (23)$$

where \bar{n} is the mean halo (galaxy) number density. The 2PCFs and therefore the mCFs are measured within the range $1 - 80 h^{-1} \text{ Mpc}$ (for details see Section 3.3).

First we study the clustering of dark matter haloes, ξ_h , (left-hand panel of Fig. 3), for our halo samples with $n_h = 3.2 \times 10^{-4} h^3 \text{ Mpc}^{-3}$. Although this statistic is not directly ob-

servable, it is instructive to study the properties of ξ_h , since this is a first step towards understanding differences in the clustering of galaxies.

The first thing we notice is that the deviation from GR does not show a monotonic dependence on $|f_{R0}|$. More explicitly, F6 and F4 models have weaker clustering than GR, while F5 haloes are more clustered than GR.

These perhaps counterintuitive results can be explained by considering the following two effects of the enhanced gravity.

Firstly, stronger gravity means a faster growth of initial density peaks, and therefore more massive structures at late times. This generally leads to a higher mean halo number density above a fixed halo mass threshold. The enhancement of halo formation is not uniform: when screening is efficient, it is stronger in low-density

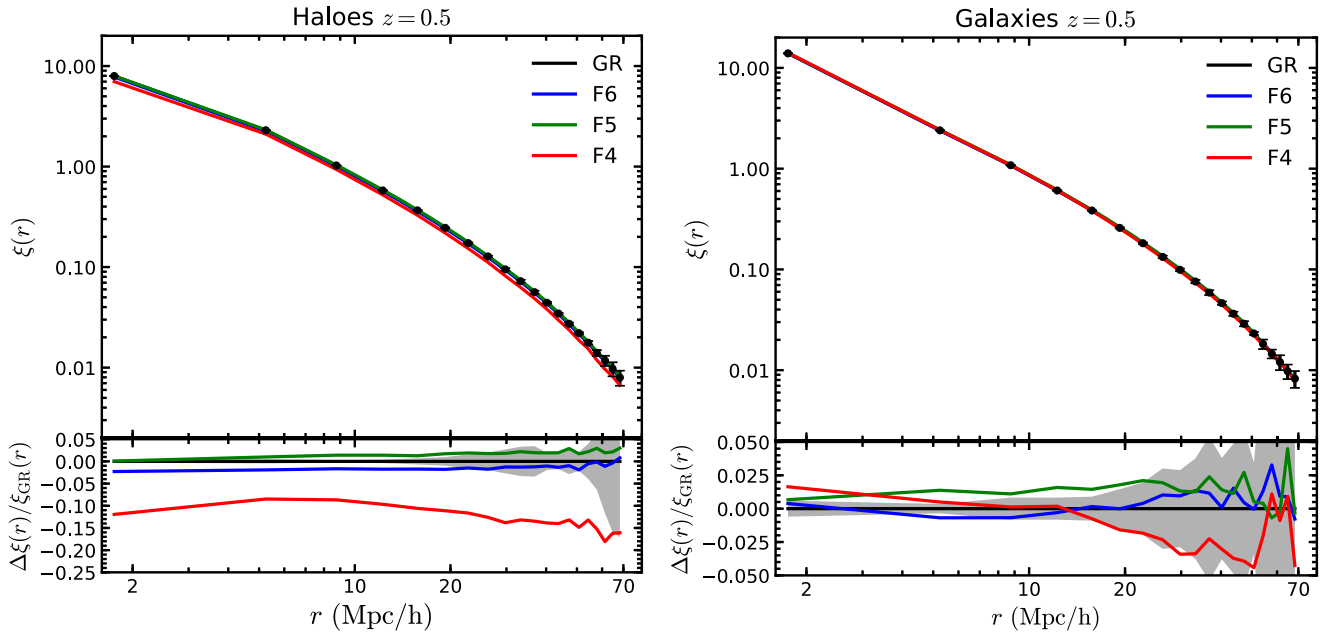


Figure 3. Two-point correlation function in real space measured for haloes (left-hand panel) with $n_h = 3.2 \times 10^{-4} h^3 \text{ Mpc}^{-3}$ and HOD galaxies (right-hand panel) in the four gravity models as labelled. The plotted values correspond to the average of the five realisations for each model. Different colour lines correspond to different gravity models as labelled. The lower subpanels show the relative difference between the results from the $f(R)$ and Λ CDM (GR) models. Error bars and shaded regions correspond to 1σ standard deviation over the five GR realisations.

regions than it is in high-density regions; when the screening is less efficient, then the growth of haloes is boosted in all environments, and those in dense regions can be boosted more because they have more matter around them to accrete.

Secondly, enhanced gravity generally leads to a stronger clustering of the structures that are formed from these initial density peaks. However, stronger gravity also means that we can expect more mergers in dense regions, reducing the number of haloes there. The latter effect can be seen by comparing the cHMFs of F5 and F4 in Fig. 1.

As we choose the halo mass cut to ensure that we consider the same number of haloes in each model any differences in ξ_h come from the different spatial distributions of haloes in the models. For F6, the deviation from GR is weak and the fifth force is suppressed in high-density regions. As a result small density peaks in low-density regions grow faster than similar density peaks in high-density regions, and more of them make it into the fixed number density halo catalogue than in GR. This makes the haloes less clustered and $\xi_h(r)$ smaller.

For F5, the enhancement of gravity is stronger and the screening is weaker, so that haloes in all regions experience faster growth; those in high-density environments have a larger supply of raw materials for accretion and growth, so that they are more likely ending up in the final halo catalogue, leading to a stronger clustering and ξ_h . For F4, the even stronger enhancement of gravity causes more mergers of haloes in dense regions to form even larger haloes, and to maintain the same \bar{n}_h more haloes in low-density regions have to be included into the halo catalogue, leading to less clustering and smaller ξ_h .

In the case of the galaxy correlation function (right-hand panel of Fig. 3), as we said before, the HOD catalogues for the $f(R)$ models were created by tuning the parameters (22; see Table 2) to approximately match the two-point correlation function in GR (to within 1–3 percent).

4.2 Marked correlation function

In this subsection we consider the marked correlations, in which one weights galaxies² by some property or ‘mark’ when estimating clustering statistics. Marked correlations are particularly well-suited to quantifying how the properties of galaxies correlate with environment (Sheth et al. 2005; Skibba et al. 2006; Skibba et al. 2009, 2012; White & Padmanabhan 2009). Here, we test the idea proposed by White (2016) that mCFs may show a clearer signature of modified gravity in the large-scale clustering of galaxies, by up-weighting low-density regions, where screening is weak and deviations from GR are strong.

The mCF is defined as (Sheth et al. 2005)

$$M(r) \equiv \frac{1}{n(r)\bar{m}^2} \sum_{ij} m_i m_j = \frac{1 + W(r)}{1 + \xi(r)}, \quad (24)$$

where the sum is over all pairs with a given separation, r , $n(r)$ is the number of such pairs and \bar{m} is the mean mark for the entire sample. In the second equality $\xi(r)$ is the two-point correlation function in which all galaxies (or haloes) are weighted equally. $W(r)$ is derived from a similar sum over galaxy (halo) pairs separated by r , as used to estimate $\xi(r)$, but now each member of the pair is weighted by the ratio of its mark to the mean mark of the full sample. The mCF, $M(r)$, can be estimated approximately using the simple pair count ratio WW/DD (where DD is the count of data–data pairs and WW represents the corresponding weighted counts). Hence, no random catalogue is needed for its computation.

The choice of the mark is flexible and depends on the application. Since we are interested in isolating the effects of the chameleon

²For simplicity, we talk about galaxies here, but the same calculation can (and will) be applied to haloes.

screening mechanism on structure formation, we study the clustering of HOD galaxies using two different definitions of environment: (a) the number density field and (b) the Newtonian gravitational potential (Shi et al. 2017).

4.2.1 Density

For this environment definition we use three marks with an adjustable dependence on density

$$m = \left(\frac{\rho_* + 1}{\rho_* + \rho_R} \right)^p, \quad (25)$$

$$m = \log_{10}(\rho_R + \rho_*), \quad (26)$$

$$m = \frac{1}{\sqrt{2\pi}\sigma_{\rho_R}} \exp\left(-\frac{(\rho_R - \rho_*)^2}{2\sigma_{\rho_R}^2}\right), \quad (27)$$

where ρ_R is the galaxy number density in units of the mean galaxy number density, $\bar{\rho}$, and p , ρ_* and σ_{ρ_R} are adjustable parameters.

A crucial step in the estimation of the mCF is the definition of the density. We measure the galaxy number density using counts-in-cells (see for e.g., Baugh, Gaztanaga & Efstathiou 1995). We divide the simulation box into cells (or cubical boxes) of the same size, and then count the number of galaxies inside each cell. Hence, we can compute the overdensity, δ , as

$$1 + \delta = \frac{N}{\bar{N}} \equiv \rho_R, \quad (28)$$

where N is the number of galaxies in each cell and \bar{N} is the mean number of galaxies in cells of a given size over the simulation volume. To compute the density we have used 60^3 cells of size $\sim 17 h^{-1}$ Mpc. Given the mean galaxy number density of CMASS galaxies, $n_g = 3.2 \times 10^{-4} h^3 \text{ Mpc}^{-3}$, we have a mean number of galaxies in the cells of $\bar{N} = 1.59$. We checked that reducing the number of cells to 30^3 – 40^3 does not affect our results significantly, while further reducing the number of cells makes the signal weaker; in the limit of 1^3 cell, $W(r)$ becomes identical to $\xi(r)$, as expected.

The first mark, equation (25), was proposed by White (2016) (hereafter the White-mark), with the motivation being that by up-weighting low-density regions (i.e. by choosing $p > 0$), one might be able to find a signature of modified gravity, since previous studies have shown that the properties of voids are different in modified gravity theories than in GR (Clampitt, Cai & Li 2013; Cai, Padilla & Li 2015; Zivick et al. 2015; Cautun et al. 2017). The log mark, equation (26), allows us to up-weight regions with $\rho_R > 1$, i.e. intermediate and high-density regions. Finally, using the Gaussian- ρ_R mark, equation (27), we are able to control the regions we want to up-weight. Previously, Llinares & McCullagh (2017) found that by using a Gaussian transformation of the density field is it possible to up-weight intermediate density regions and find bigger differences between the clustering of objects in modified gravity and GR models. Keeping this in mind, we use the Gaussian- ρ_R mark to up-weight only intermediate density regions.

It is evident that by using equation (25) one can control the up-weighting by varying the power p and the parameter ρ_* . For simplicity we chose $p = 1$ and $\rho_* = 10^{-6}$. With the log-mark, a natural choice of the parameter which controls the enhancement is $\rho_* = 1$, given $m = 0$ for voids ($\rho_R = 0$). The parameters we chose for the Gaussian- ρ_R mark are: $\rho_* = 1.5$ and $\sigma_{\rho_R} = 0.2$, which ensures that we up-weight intermediate-density regions of interest. The functional form of the marks, equations (25)–(27), is shown

in the left-hand panels of Fig. 4. We have tried using different values of p , ρ_R , and ρ_* but found that our results do not show significant differences on varying these parameters. We refer to low-, intermediate-, and high-density regions as those for which the cells contain $N = 1$, 2 – 3 , and >4 objects or, equivalently, to cells with $\rho_R = 0.62$, 1.25 – 1.88 , and >2.51 , respectively (see equation 28).

Fig. 4 shows the mCFs at $z = 0.5$ measured from the halo (middle panels) and the HOD (left-hand panels) catalogues in the $f(R)$ and GR models. In all cases the mCF goes to unity on large scales as expected (see right-hand expression of equation 24). The first row of plots in Fig. 4 shows the mCF using the mark defined by equation (25), the White-mark, with $p = 1$ and $\rho_* = 10^{-6}$, the second row shows the log-mark, equation (26) with $\rho_* = 1$, and the third row shows the Gaussian- ρ_R mark with $\rho_* = 1.5$ and $\sigma_{\rho_R} = 0.2$. We observe different behaviours: for the White-mark, equation (25), the mCF is $M(r) \leq 1$ at small separations, for the log-mark, equation (26), we have $M(r) \geq 1$, while for the Gaussian- ρ_R we notice a transition from $M(r) \leq 1$ to $M(r) > 1$ at intermediate scales.

Analysing the behaviour of the halo mCFs (see middle panel of Fig. 4) we find the following features:

- (i) The clustering of F6 is almost indistinguishable from that of GR for all three marks, because of the efficient screening.
- (ii) For F5, the stronger growth (see Section 4.1) means more clustering of haloes on small scales, which is why $W(r)$ and therefore the mCF is more affected at smaller r .
- (iii) In the case of F4, the higher production rate of massive haloes, driven by the more frequent mergers of lower mass haloes (see Section 4.1), leads to the incorporation of haloes into the fixed number density sample which correspond to low density peaks and which are more likely to come from low-density regions. Hence, the probability of finding a pair of tracers (haloes or galaxies) increases at intermediate separation r due to presence of these low-mass haloes.

The right columns of Fig. 4 show that galaxies qualitatively mimic the marked clustering of haloes (at least for the White and log marks). Hence, the behaviour of the galaxy mCFs can be understood following the same explanation as presented above for haloes. It is interesting to notice that even with the added complexity of populating haloes with HOD galaxies, the qualitative behaviour of the mCFs preserves, suggesting that a true physical feature is being observed here.

For the Gaussian- ρ_R mark, equation (27), which enhances intermediate-density regions (cells with 2 or 3 haloes/galaxies), we found that the F4 galaxy mCF reaches a maximum of 20 per cent for the lowest separation bin, while F6 predicts a difference of 5 per cent and F5 keeps closer to GR with a difference of ~ 3 per cent.

4.2.2 Gravitational potential

Our second definition of environment is based on the Newtonian gravitational potential produced by dark matter haloes. The dark matter haloes in our simulations are reasonably well described by a NFW density profile (Navarro et al. 1996, 1997)

$$\rho_{\text{NFW}} = \frac{\rho_s}{(r/r_s)(1 + r/r_s)^2}, \quad (29)$$

where r_s is the scale radius where the profile has a slope of -2 and ρ_s is the characteristic density. The Newtonian gravitational potential is obtained by solving the Poisson equation, $\nabla^2 \Phi_N = 4\pi G \rho_{\text{NFW}}$,

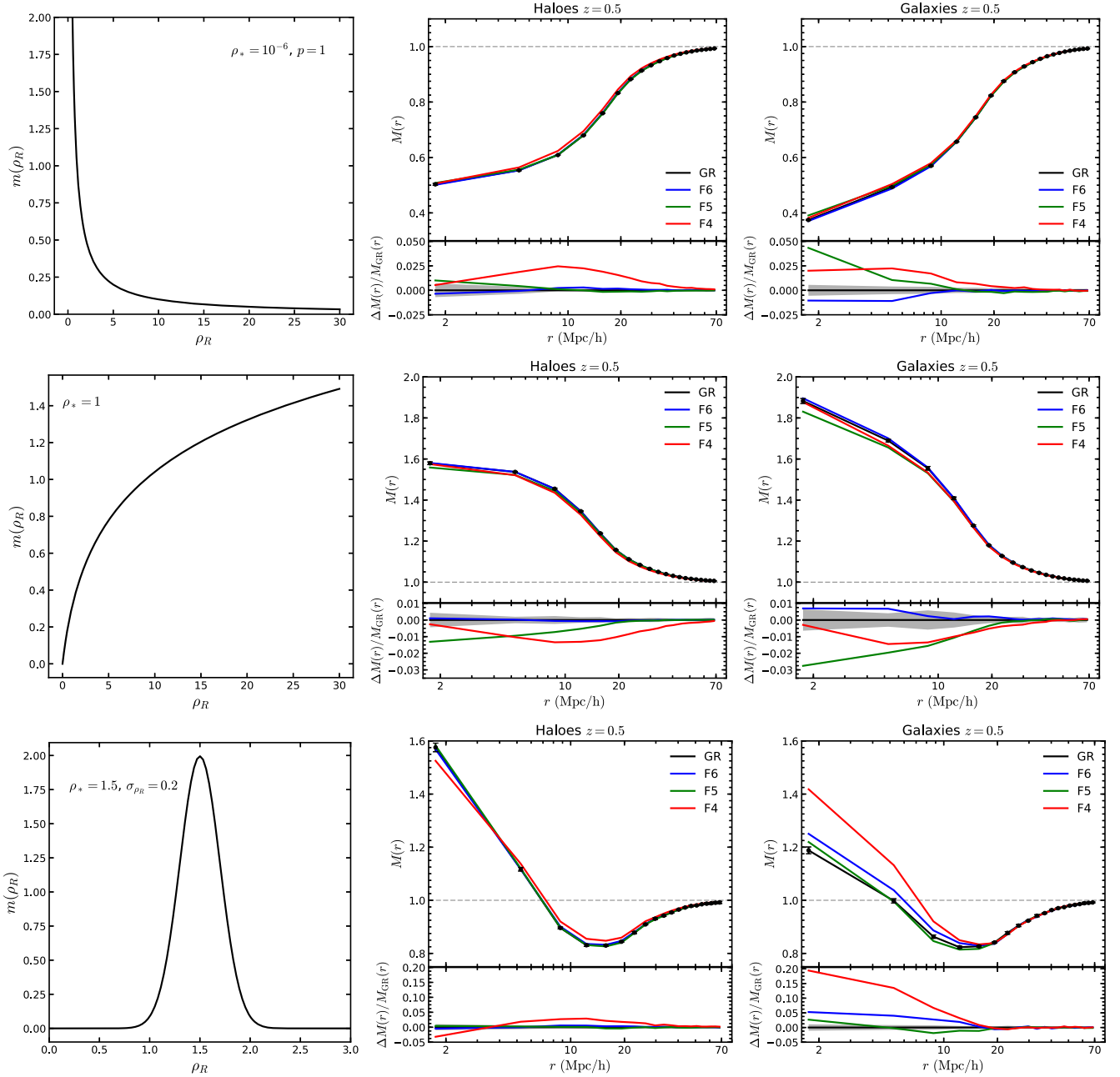


Figure 4. mCFs of haloes and CMASS galaxies at $z = 0.5$; mark in function of number density field. Left: functional form of the mark in function of density field, middle: halo mCFs and right: galaxy mCFs. Plots from upper to bottom: White-mark (25), log-mark (26), and Gaussian- ρ_R mark (27). All lower subpanels show the relative difference between $f(R)$ models and GR. The plotted values correspond to the average over the five realisations. Errors correspond to 1σ standard deviation over the five GR realisations.

for the NFW density profile equation (29) (Cole & Lacey 1996; Navarro et al. 1997; Lokas & Mamon 2001)

$$\Phi_N = -\frac{GM_{200c}}{r_{200c}} \frac{\ln(1+c)}{\ln(1+c) - c/(1+c)}, \quad (30)$$

where G is Newton's gravitational constant, M_{200c} was defined in equation (16) and c is the concentration parameter defined as $c \equiv r_{200c}/r_s$. Previous studies have used the Newtonian gravitational potential in modified gravity to characterize local variations in the strength of gravity (see e.g. Cabre et al. 2012; Stark et al. 2016; Shi et al. 2017).

For this environment definition we define a Gaussian mark which allows us to up-weight galaxies in some regions of interest,

$$m = \frac{1}{\sqrt{2\pi}\sigma_\Phi} \exp \left[-\frac{(\log_{10}(|\Phi_N|) - \Phi_*)^2}{2\sigma_\Phi^2} \right], \quad (31)$$

where Φ_* and σ_Φ are free parameters of the mark which control the amplitude and width of the regions highlighted. As we can see from the distribution of galaxies as a function of host halo mass (right-hand panel of Fig. 2), most galaxies live in haloes with masses between $10^{13} < M_{200c}/[h^{-1} M_\odot] < 10^{14}$ (which correspond to the mass range of groups of galaxies). Hence, we use the Gaussian- Φ_N

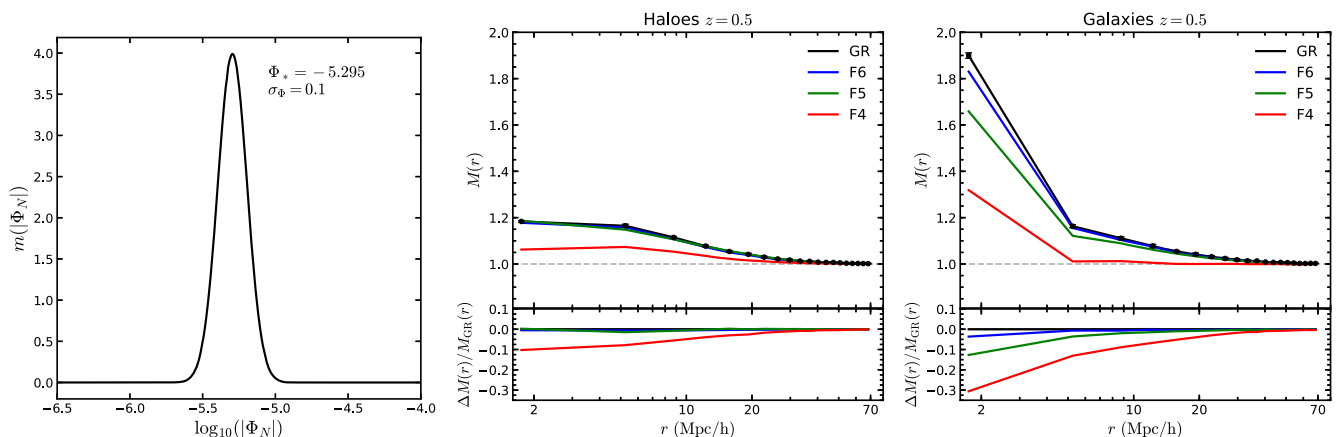


Figure 5. mCFs of haloes and CMASS galaxies at $z = 0.5$; mark in function of the Newtonian gravitational potential. Left-hand side panel shows the functional form of the Gaussian- Φ_N mark (31); the values of the parameters Φ_* and σ_Φ are shown in the legend. Middle and right-hand side plots show the mCF using the mark given by equation (31) for haloes and galaxies, respectively. All lower subpanels for middle and right-hand side plots show the relative difference between $f(R)$ models and GR. The plotted values correspond to the average over the five realisations. Errors correspond to 1σ standard deviation over the five GR realisations.

mark to up-weight galaxies contained in these haloes. In principle we should be able to find a bigger difference in the clustering between the GR and $f(R)$ models using this mark, as suggested by the cumulative HMF (lower panel of Fig. 1).

The value of the centre of the Gaussian is $\Phi_* = -5.295$. This value was found by computing the Newtonian gravitational potential for each galaxy in Box 1 for GR, then we pick the maximum value found for haloes with $M_{200c} = 10^{14} h^{-1} M_\odot$ (Φ_{\max}) and the minimum value for haloes with $M_{200c} = 10^{13} h^{-1} M_\odot$ (Φ_{\min}), finally we take $\Phi_* = (\Phi_{\max} + \Phi_{\min})/2$. We tried different values of the width, finding that $\sigma_\Phi = 0.1$ best ensures that we only up-weight galaxies in the haloes of interest. The functional form of the Gaussian- Φ_N mark, equation (31), is shown in the left-hand panel of Fig. 5.

The halo and galaxy mCF is presented in the middle and right-hand panels of Fig. 5, respectively. The results can be summarized as follows:

(i) In the case of the halo/galaxy mCF (middle and right panels of Fig. 5, respectively), the two-point correlation function (used as the denominator of equation 24) is lower than the weighted correlation function, leading to $M(r) \geq 1$ for all gravity models, due to the stronger clustering of the up-weighted haloes in the mass range $M_{200c}/[h^{-1} M_\odot] = [10^{13}, 10^{14}]$.

(ii) F6 predicts almost an identical halo/galaxy marked clustering to that in GR, which is consistent to our understanding that the screening mechanism in this model works efficiently in haloes of the mass range up-weighted.

(iii) For F4 haloes, the mCF is higher than the 2PCF for the reason given in the first bullet point above. However, in this model a larger fraction of haloes in the mass range $M_{200c}/[h^{-1} M_\odot] \in [10^{13}, 10^{14}]$ are formed from low initial density peaks (due to stronger gravity) which are not very strongly clustered, such that the up-weighting of them – while making $M(r) \geq 1$ – does not lead to a $M(r)$ as large as in GR. This leads to $\Delta M(r)/M_{GR}(r) < 0$ for F4. For F5 haloes, the fifth force is strong enough to enhance their clustering, but not too strong to produce excessive merging, and so the up-weighting using the Gaussian mark increases the mCF as significantly as in GR.

(iv) For galaxies, a key difference from haloes is that a halo can host several galaxies while some haloes do not host galaxies at all. In F4 and F5, more relatively low initial density peaks have been promoted to the halo mass range $M_{200c}/[h^{-1} M_\odot] \in [10^{13}, 10^{14}]$ due to the enhanced gravity, and at the same time some high density peaks have grown out of this mass range. This means that if we up-weight galaxies whose host haloes are in this mass range, we end up with more central and fewer satellite galaxies, and more of them are hosted by haloes from lower initial density peaks. By the same reasoning as above, while we still have $M(r) > 1$ for these models, it is smaller than in GR and F6. In particular, we have noticed that $\Delta M(r)/M_{GR}(r)$ reaches 5–10 percent for F5 and 20–30 percent for F4 in $r = 2\text{--}5 h^{-1} \text{ Mpc}$. These results are very stable, and change very little across the different simulation realisations.

Also we note that the differences between the $f(R)$ and GR models are boosted when we use additional information to the density field. This can be seen by comparing the right-hand panels of Fig. 4 with the right-hand panel of Fig. 5. The differences get larger in such cases because the galaxy density field and galaxy distribution have been tuned to match between the different models (see Section 3.3). In all cases we observe that signals above $20 h^{-1} \text{ Mpc}$ become identical between models. This is because the mCF is the ratio of two correlation functions (see right-hand expression of equation 24) and we have $\xi(r) \sim W(r)$ for $r > 20 h^{-1} \text{ Mpc}$.

From the observational point of view, we can measure the Newtonian gravitational potential from the X-ray temperature of galaxy clusters (see e.g. Allen et al. 2004, 2008; Li, He & Gao 2016), the gas mass fractions of clusters and the escape velocity profile, $v_{\text{esc}}(r)$ (Stark et al. 2016). Hence, if we reconstruct the gravitational potential from the observations mentioned above and use a mark that is a function of the potential, similar to equation (31), then we can test this approach and potentially find a measurable signature of modified gravity. One caveat is that the gravitational potential constructed in this way is the dynamical potential, while in this study we have used lensing potential of haloes (see e.g. He & Li 2016).

5 DISCUSSION AND CONCLUSIONS

We study the clustering of haloes and galaxies in four different cosmologies: a Λ CDM model which is based on GR and three Hu & Sawicki $f(R)$ chameleon models with fixed $n = 1$ and $|f_{R0}| = 10^{-6}, 10^{-5}, 10^{-4}$ (denoted F6, F5, and F4). We analyse the output of dark matter-only N -body simulations related to these models at $z = 0.5$.

First, we study the cHMF, finding that the F4 model predicts more haloes than GR at all masses probed by our simulations, with the maximum difference reaching an excess of more than 50 per cent for haloes with mass $M_{200c} > 10^{14.3} h^{-1} M_{\odot}$. These differences occur due to the enhancement of gravity in $f(R)$ gravity, which results in the production of more massive haloes in F4 than GR through faster accretion and more frequent merging of small haloes. The differences found in F5 reach 25 per cent for haloes with masses $10^{13} h^{-1} M_{\odot} < M_{200c} < 10^{14} h^{-1} M_{\odot}$ where the screening mechanism at this mass scale is inefficient for this model. F6 shows the smallest difference from GR because in this model the chameleon screening is strong in haloes with mass $M_{200c} > 10^{13} h^{-1} M_{\odot}$, thereby suppressing the effects of the fifth force.

We populate dark matter haloes with galaxies using a HOD, using a five-parameter model which treats separately central and satellite galaxies, with the values of the parameters as used in Manera et al. (2012) to reproduce the clustering of CMASS galaxies with a density number, $n_g = 3.2 \times 10^{-4} h^3 \text{ Mpc}^{-3}$ (Anderson et al. 2012) for our GR simulations. We tuned the parameters to match the galaxy number density and two-point correlation function of GR to within 1–3 per cent for the $f(R)$ models. The galaxy 2PCFs for the $f(R)$ and GR models are presented in the right plot of Fig. 3.

Then we study the two-point clustering of dark matter haloes. We choose samples of haloes with fixed halo number density, $n_h = n_g$, resulting to different mass cutoffs in our halo catalogues for all gravity models: $7.643 \times 10^{12} h^{-1} M_{\odot}$ (GR), $7.798 \times 10^{12} h^{-1} M_{\odot}$ (F6), $9.124 \times 10^{12} h^{-1} M_{\odot}$ (F5), and $8.734 \times 10^{12} h^{-1} M_{\odot}$ (F4). We find significant differences in the clustering of dark matter haloes for $f(R)$ models with respect to the GR predictions. The maximum difference between F4 and GR is ~ 20 per cent, while for F5 and F6 it is less than 5 per cent. Also we note that haloes in F5 are more clustered than those haloes in the Λ CDM model, whereas for F6 and F4 haloes are less clustered than their GR counterparts. These results are the effects of the enhancement of gravity which means a stronger growth of density peaks and therefore more massive structures at late times which gives a stronger clustering of the structures that are formed from these density peaks.

To investigate whether or not these differences could be boosted by using an alternative approach to measure galaxy clustering, we used the mCF (Sheth et al. 2005; White 2016). For this purpose we use two definitions for the environment of galaxies/haloes: (a) the number density field and (b) the Newtonian gravitational potential of the host halo. For the former we analyse three marks: (i) an inverse power law which enhances low-density regions (see equation 25), (ii) a log-transform mark which up-weights intermediate- and high-density regions (see equation 26), and (iii) a Gaussian mark given by equation (31) which allows us to up-weight only intermediate-density regions, $\rho_R = 1.25$ – 1.88 . For the latter we use a Gaussian mark which allows us to up-weight haloes (and galaxies within those haloes) with mass $10^{13} < M_{200c}/[h^{-1} M_{\odot}] < 10^{14}$.

We found that the halo and galaxy mCFs for F6 is indistinguishable from GR using all marks, except for the galaxy Gaussian (ρ_R and Φ_N) mCFs which predict differences at most ~ 5 per cent from GR. For the F5 (F4) model, we notice that galaxies mimic

the marked clustering at least for the White and log density-marks finding differences of 5 per cent (2.5 per cent) and 2.5 per cent (2.5 per cent), respectively. On the other hand, we observe that with the Gaussian marks (density field and gravitational potential) the difference in the galaxy mCF is boosted, especially for F4, producing a difference of 20 per cent (using density field) and 30 per cent (using gravitational potential) with respect GR.

The galaxy mCFs show smaller differences between the $f(R)$ and GR models for the density marks, equations (25)–(27), than in the case when using the gravitational potential mark, equation (31), this is because the galaxy density field has been tuned to match between the different models. One caveat for our results is that there will be systematics when estimating the mark for observational samples.

Another important feature we observe from mCFs is that the signal above $20 h^{-1} \text{ Mpc}$ does not distinguish between models (see corresponding plots of Figs. 4 and 5). Instead, the measurable differences are on small scales. To improve our predictions on sub-Mpc scales we need to perform higher resolution simulations, but we leave this for future work.

Valogiannis & Bean (2017) recently found that using the dark matter distribution and the White-mark, equation (25) with $\rho_* = 4$ and $p = 10$, the difference between F4 and GR mCFs can reach a maximum of 37 per cent at $r = 1.81 h^{-1} \text{ Mpc}$. These results cannot readily be compared with ours, since we consider dark matter haloes and galaxies rather than the dark matter itself. Furthermore, we employ a different definition of density (counts-in-cells versus the cloud-in-cell smoothing used by Valogiannis & Bean). Although their simulations are similar resolution to the ones we use, the volume of our boxes is ~ 60 times larger, which allows more robust clustering measurements.

If we consider the statistical errors presented in this paper, then the differences between the $f(R)$ signals with respect GR are significant. It should be feasible to test the differentiating power of marked clustering statistics using real data from current galaxy surveys. In future work we need to improve the resolution of the simulations and make more realistic mock galaxy catalogues to allow a fairer comparison with upcoming observations.

Here we have demonstrated the potential of the mCF to differentiate between gravity models. The next step is to extend these calculations, which were presented for massive galaxies, to the emission line galaxies that will be selected by the DESI and *Euclid* redshift surveys.

ACKNOWLEDGEMENTS

The authors wish to thank Lee Stothert for providing the code to compute the two-point correlation functions and the weighted number counts. Also we would like to thank the referee for their positive and helpful comments about our paper. CH-A is supported by the Mexican National Council of Science and Technology (CONACyT) through grant No. 286513/438352. BL is supported by the European Research Council (ERC-StG-716532-PUNCA). This project has received funding from the European Union's Horizon 2020 Research and Innovation Programme under the Marie Skłodowska-Curie grant agreement No 734374, LACEGAL. We acknowledge support from STFC Consolidated Grants ST/P000541/1, ST/L00075X/1. This work used the DiRAC Data Centric system at Durham University, operated by the Institute for Computational Cosmology on behalf of the STFC DiRAC HPC Facility (www.dirac.ac.uk). This equipment was funded by BIS National E-infrastructure capital grant ST/K00042X/1, STFC capital grants ST/H008519/1, and

ST/K00087X/1, STFC DiRAC Operations grant ST/K003267/1 and Durham University. DiRAC is part of the National E-Infrastructure.

REFERENCES

- Ade P. A. R. et al., 2014, *A&A*, 571, A16
- Ade P. A. R. et al., 2016, *A&A*, 594, A13
- Aghamousa A. et al., 2016, preprint ([arXiv:1611.00036](https://arxiv.org/abs/1611.00036))
- Allen S. W., Schmidt R. W., Ebeling H., Fabian A. C., van Speybroeck L., 2004, *Mon. Not. Roy. Astron. Soc.*, 353, 457
- Allen S. W., Rapetti D. A., Schmidt R. W., Ebeling H., Morris G., Fabian A. C., 2008, *Mon. Not. Roy. Astron. Soc.*, 383, 879
- Anderson L. et al., 2012, *MNRAS*, 427, 3435
- Armijo J., Cai Y.-C., Padilla N., Li B., Peacock J. A., 2018, *MNRAS*, 478, 3627
- Arnalte-Mur P., Hellwing W. A., Norberg P., 2017, *Mon. Not. Roy. Astron. Soc.*, 467, 1569
- Barreira A., Bose S., Li B., 2015, *JCAP*, 1512, 059
- Baugh C. M., 2006, *Rept. Prog. Phys.*, 69, 3101
- Baugh C. M., Gaztanaga E., Efstathiou G., 1995, *MNRAS*, 274, 1049
- Behroozi P. S., Wechsler R. H., Wu H.-Y., 2013, *Astrophys. J.*, 762, 109
- Benson A. J., 2010, *Phys. Rep.*, 495, 33
- Berlind A. A., Weinberg D. H., 2002, *Astrophys. J.*, 575, 587
- Bose S., Hellwing W. A., Li B., 2015, *JCAP*, 1502, 034
- Bose S., Li B., Barreira A., He J.-h., Hellwing W. A., Koyama K., Llinares C., Zhao G.-B., 2017, *JCAP*, 1702, 050
- Brax P., van de Bruck C., Davis A.-C., Shaw D. J., 2008, *Phys. Rev.*, D78, 104021
- Cabre A., Vikram V., Zhao G.-B., Jain B., Koyama K., 2012, *JCAP*, 1207, 034
- Cai Y.-C., Padilla N., Li B., 2015, *Mon. Not. Roy. Astron. Soc.*, 451, 1036
- Carroll S. M., Duvvuri V., Trodden M., Turner M. S., 2004, *Phys. Rev.*, D70, 043528
- Cataneo M. et al., 2015, *Phys. Rev.*, D92, 044009
- Cataneo M., Rapetti D., Lombriser L., Li B., 2016, *JCAP*, 1612, 024
- Cautun M., Paillas E., Cai Y.-C., Bose S., Armijo J., Li B., Padilla N., 2017, *MNRAS*, 476, 3195
- Ceron-Hurtado J. J., He J.-h., Li B., 2016, *Phys. Rev.*, D94, 064052
- Clampitt J., Cai Y.-C., Li B., 2013, *MNRAS*, 431, 749
- Cole S., Lacey C., 1996, *MNRAS*, 281, 716
- Cole S., Lacey C. G., Baugh C. M., Frenk C. S., 2000, *Mon. Not. Roy. Astron. Soc.*, 319, 168
- Conroy C., Wechsler R. H., Kravtsov A. V., 2006, *Astrophys. J.*, 647, 201
- Cooray A., Milosavljevic M., 2005, *Astrophys. J.*, 627, L89
- Copeland E. J., Sami M., Tsujikawa S., 2006, *Int. J. Mod. Phys.*, D15, 1753
- Dark Energy Survey Collaboration, 2016, *MNRAS*, 460, 1270
- De Felice A., Tsujikawa S., 2010, *Living Rev. Rel.*, 13, 3
- Fontanot F., Puchwein E., Springel V., Bianchi D., 2013, *MNRAS*, 436, 2672
- He J.-h., Li B., 2016, *Phys. Rev. D*, 93, 123512
- Hinshaw G. et al., 2013, *Astrophys. J. Suppl.*, 208, 19
- Hu W., Sawicki I., 2007, *Phys. Rev.*, D76, 064004
- Jennings E., Baugh C. M., Li B., Zhao G.-B., Koyama K., 2012, *Mon. Not. Roy. Astron. Soc.*, 425, 2128
- Joyce A., Jain B., Khoury J., Trodden M., 2015, *Phys. Rep.*, 568, 1
- Khoury J., Weltman A., 2004, *Phys. Rev.*, D69, 044026
- Klypin A., Prada F., Yepes G., Gottlober S., 2013, preprint ([arXiv:1310.3740](https://arxiv.org/abs/1310.3740))
- Koyama K., 2016, *Rep. Prog. Phys.*, 79, 046902
- Kravtsov A. V., Berlind A. A., Wechsler R. H., Klypin A. A., Gottloeber S., Allgood B., Primack J. R., 2004, *Astrophys. J.*, 609, 35
- Laureijs R. et al., 2011, preprint ([arXiv:1110.3193](https://arxiv.org/abs/1110.3193))
- Li B., Zhao G.-B., Teyssier R., Koyama K., 2012, *JCAP*, 1201, 051
- Li B., Hellwing W. A., Koyama K., Zhao G.-B., Jennings E., Baugh C. M., 2013, *Mon. Not. Roy. Astron. Soc.*, 428, 743
- Li B., He J.-h., Gao L., 2016, *Mon. Not. Roy. Astron. Soc.*, 456, 146
- Liu X. et al., 2016, *Phys. Rev. Lett.*, 117, 051101
- Llinares C., McCullagh N., 2017, *MNRAS*, 472, L80
- Lokas E. L., Mamon G. A., 2001, *Mon. Not. Roy. Astron. Soc.*, 321, 155
- Lombriser L., 2014, *Ann. Phys.*, 526, 259
- Lombriser L., Li B., Koyama K., Zhao G.-B., 2013, *Phys. Rev.*, D87, 123511
- Lombriser L., Simpson F., Mead A., 2015, *Phys. Rev. Lett.*, 114, 251101
- Manera M. et al., 2012, *Mon. Not. Roy. Astron. Soc.*, 428, 1036
- Mota D. F., Shaw D. J., 2007, *Phys. Rev.*, D75, 063501
- Murray S. G., Power C., Robotham A. S. G., 2013, *Astron. Comput.*, 3, 23
- Navarro J. F., Frenk C. S., White S. D. M., 1996, *Astrophys. J.*, 462, 563
- Navarro J. F., Frenk C. S., White S. D. M., 1997, *Astrophys. J.*, 490, 493
- Nelder J. A., Mead R., 1965, *Comput. J.*, 7, 308
- Peacock J. A., Smith R. E., 2000, *Mon. Not. Roy. Astron. Soc.*, 318, 1144
- Peebles P. J. E., 1980, *The Large-scale Structure of the Universe*, Princeton University Press
- Press W. H., Schechter P., 1974, *Astrophys. J.*, 187, 425
- Prunet S., Pichon C., Aubert D., Pogossyan D., Teyssier R., Gottloeber S., 2008, *Astrophys. J. Suppl.*, 178, 179
- Reddick R. M., Wechsler R. H., Tinker J. L., Behroozi P. S., 2013, *Astrophys. J.*, 771, 30
- Reid B. A. et al., 2010, *Mon. Not. Roy. Astron. Soc.*, 404, 60
- Schaye J., Crain R. A., Bower R. G., Furlong M., Schaller M. et al., 2015, *Mon. Not. Roy. Astron. Soc.*, 446, 521
- Schmidt F., Lima M. V., Oyaizu H., Hu W., 2009, *Phys. Rev.*, D79, 083518
- Sheth R. K., Connolly A. J., Skibba R., 2005, preprint ([arXiv:astro-ph/0511773](https://arxiv.org/abs/astro-ph/0511773))
- Shi D., Li B., Han J., 2017, *Mon. Not. Roy. Astron. Soc.*, 469, 705
- Skibba R., Sheth R. K., Connolly A. J., Scranton R., 2006, *Mon. Not. Roy. Astron. Soc.*, 369, 68
- Skibba R. A. et al., 2009, *Mon. Not. Roy. Astron. Soc.*, 399, 966
- Skibba R. A. et al., 2012, *Mon. Not. Roy. Astron. Soc.*, 423, 1485
- Somerville R. S., Primack J. R., 1999, *Mon. Not. Roy. Astron. Soc.*, 310, 1087
- Sotiriou T. P., Faraoni V., 2010, *Rev. Mod. Phys.*, 82, 451
- Stark A., Miller C. J., Kern N., Gifford D., Zhao G.-B., Li B., Koyama K., Nichol R. C., 2016, *Phys. Rev.*, D93, 084036
- Teyssier R., 2002, *Astron. Astrophys.*, 385, 337
- Tinker J. L., Robertson B. E., Kravtsov A. V., Klypin A., Warren M. S., Yepes G., Gottloeber S., 2010, *Astrophys. J.*, 724, 878
- Vale A., Ostriker J. P., 2004, *Mon. Not. Roy. Astron. Soc.*, 353, 189
- Valogiannis G., Bean R., 2017, *Phys. Rev. D*, 97, 023535
- Vogelsberger M., Genel S., Springel V., Torrey P., Sijacki D. et al., 2014, *Nature*, 509, 177
- Wang J., Hui L., Khoury J., 2012, *Phys. Rev. Lett.*, 109, 241301
- Weinberg D. H., Bullock J. S., Governato F., Kuzio de Naray R., Peter A. H. G., 2014, *Proc. Nat. Acad. Sci.*, 112, 12249
- White M., 2016, *JCAP*, 1611, 057
- White M., Padmanabhan N., 2009, *Mon. Not. Roy. Astron. Soc.*, 395, 2381
- White M. et al., 2011, *ApJ*, 728, 126
- Winther H. A., Mota D. F., Li B., 2012, *Astrophys. J.*, 756, 166
- Winther H. A. et al., 2015, *Mon. Not. Roy. Astron. Soc.*, 454, 4208
- Yang X.-h., Mo H. J., van den Bosch F. C., 2003, *Mon. Not. Roy. Astron. Soc.*, 339, 1057
- Zhao G.-B., Li B., Koyama K., 2011, *Phys. Rev. Lett.*, 107, 071303
- Zheng Z. et al., 2005, *Astrophys. J.*, 633, 791
- Zheng Z., Coil A. L., Zehavi I., 2007, *Astrophys. J.*, 667, 760
- Zivick P., Sutter P. M., Wandelt B. D., Li B., Lam T. Y., 2015, *Mon. Not. Roy. Astron. Soc.*, 451, 4215

This paper has been typeset from a \LaTeX file prepared by the author.